



## Research article

## Calibration and validation of the HydroColor and Citclops smartphone applications for water quality monitoring

Peter N-jonaam Mahama<sup>a,b,\*</sup>, Suhyb Mohammed Salama<sup>c</sup><sup>a</sup> Public Health Division, 37 Military Hospital, Accra, Ghana<sup>b</sup> Ghana Level II Plus Hospital, United Nations Interim Security Force for Abyei, Abyei<sup>c</sup> Department of Water Resources and Environmental Management, Faculty of Geo-Information Science and Earth Observation, University of Twente, Enschede, the Netherlands

## ARTICLE INFO

## Keywords:

Applications (APPs)

Colour

Smartphone image

Citclops

HydroColor

Concentration of suspended particulate materials ([SPM])

Turbidity

## ABSTRACT

Water quality monitoring, essential for safeguarding ecosystems and human health, has gained increasing significance as societies worldwide prioritize environmental awareness and sustainable practices. Therefore, this study evaluates the performance of two smartphone applications (APPs), HydroColor and Citclops (now EyeOnWater), in estimating water quality parameters such as turbidity, the concentration of suspended particulate matter ([SPM]), and colour. By comparing laboratory and hyperspectral sensors measurements with water quality parameters estimated from smartphone images, the study assessed the accuracy and efficiency of the transfer functions employed by these APPs. The study findings revealed varying degrees of accuracy, with HydroColor  $R^2$  values of 0.36 and 0.83 for turbidity and [SPM], respectively, while Citclops achieved an  $R^2$  value of 0.7 for colour estimation. The study identified limitations in both APPs, particularly in their applicability to different water systems. These insights underscore the importance of proper calibration and validation procedures for smartphone-based water quality monitoring APPs. Also, the findings underscore the growing significance of smartphone APPs in enabling accessible and real-time monitoring of water quality, highlighting their potential to revolutionize the democratization of environmental monitoring practices through citizen science. Ultimately, this research contributes to the advancement of smartphone-based monitoring initiatives to inform decision-making processes in environmental management, and enhancing our understanding of water quality dynamics in diverse environments.

## 1. Introduction

Environmental sensing and monitoring have become increasingly pivotal as societies worldwide strive for greater environmental awareness and sustainable practices. This growing emphasis is reflected in the increasing global market for environmental monitoring, which was valued at \$14 billion in 2022 and is forecasted to reach \$19.3 billion by 2030 [1]. Among the many facets of environmental monitoring, water quality assessment holds particular significance, given water's fundamental role in ecosystems and human well-being. Deteriorating water quality not only poses immediate threats to human health but also undermines ecological integrity, making robust and innovative monitoring initiatives imperative [2].

\* Corresponding author. Public Health Division, 37 Military Hospital, Accra, Ghana.  
E-mail address: [mpnjonaam@gmail.com](mailto:mpnjonaam@gmail.com) (P.N.-j. Mahama).

<https://doi.org/10.1016/j.heliyon.2024.e30100>

Received 10 January 2024; Received in revised form 18 April 2024; Accepted 19 April 2024

Available online 23 April 2024

2405-8440/© 2024 The Authors. Published by Elsevier Ltd. This is an open access article under the CC BY-NC-ND license (<http://creativecommons.org/licenses/by-nc-nd/4.0/>).

In this context, the demand for near-real-time analysis of water quality has intensified, driven by the need for timely and actionable data. Optical remote sensing technologies have emerged as powerful tools in this endeavour, facilitating the transition from traditional laboratory-based analyses to dynamic, spatially explicit monitoring approaches [3]. This evolution has been enabled by a diverse array of platforms, including satellites [3], aircraft [4], drones [5], and increasingly, smartphones [6]. The ubiquity of smartphones and their sophisticated imaging capabilities make them particularly promising for democratizing environmental monitoring efforts, empowering citizens to actively engage in data collection and analysis.

Among the various APPs harnessing smartphone technology for water quality assessment, HydroColor and Citclops (now Eye-OnWater) stand out as pioneering platforms. Leveraging smartphone cameras, these APPs capture red, green, and blue (RGB) images of water surfaces and employ algorithms to first derive their transfer functions (colour space). The HydroColor APP uses the RGB channels of the smartphone images taken of a grey card, sky, and water surface to convert to remote sensing reflectance  $R_{rs}(RGB)$  [7]. Using specific models, the  $R_{rs}(RGB)$  is then used to estimate turbidity, [SPM], and colour. The Citclops APP uses the RGB channels of a smartphone water surface image only to derive the  $xyz$  chromaticity coordinates. These chromaticity coordinates are then subsequently converted to the hue colour angle  $\alpha_p(^{\circ})$  which is used to index the colour of the water image as the Forel-Ule Index (FUI) [8]. While both APPs utilize similar input data, their underlying transfer functions differ significantly, leading to variations in the accuracy and efficiency of their estimations.

Despite the increasing adoption of smartphone-based water quality monitoring, there remains a notable gap in the literature regarding the comparative evaluation of transfer functions employed by different APPs. Addressing this gap is crucial for enhancing the reliability and robustness of smartphone-based monitoring systems, thereby facilitating informed decision-making and resource management strategies. Consequently, this study aims to fill this void by rigorously assessing the efficiency and accuracy of transfer functions utilized by HydroColor and Citclops APPs. By elucidating the strengths and limitations of these approaches, this research endeavours to contribute valuable insights to the increasing field of smartphone-based water quality monitoring.

Innovatively, this study not only evaluates the performance of existing smartphone APPs but also identifies avenues for enhancing their effectiveness through refined calibration and validation procedures. By elucidating the nuances of transfer functions and their impact on estimation accuracy, this research lays the groundwork for future advancements in smartphone-based water quality monitoring, thereby facilitating more comprehensive and reliable environmental assessments.

## 2. Methodology

### 2.1. Study areas and data sets

The research was carried out using four surface water resources (three lakes and an artificial wetland) in The Netherlands. The first two lakes from the first field campaign; Binnenschelde Lake and Markiezaatsmeer Lake are neighbouring water bodies located southwestern of The Netherlands as shown in the Google Earth map of Fig. 1. The second phase of the study was at Hulsbeek Lake and Kristalbad artificial wetland located at the eastern part of The Netherlands. An example of the sampling points is as shown in Fig. 2 for Kristalbad artificial wetland.

Measurements were carried out under the following weather conditions; overcast clouds and strong wind (Binnenschelde Lake),

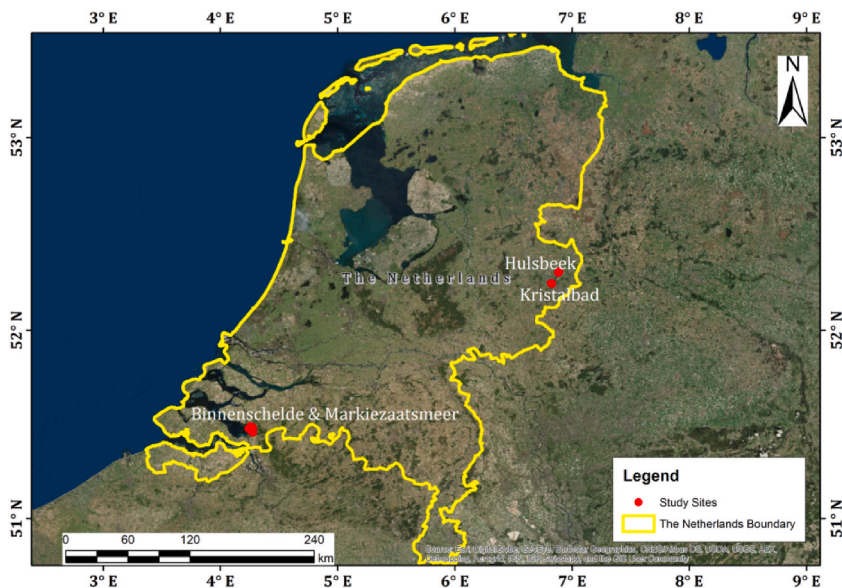


**Fig. 1.** Google Earth map showing the overlaid study sites (red dots) in The Netherlands country boundary (yellow line). (For interpretation of the references to colour in this figure legend, the reader is referred to the Web version of this article.)

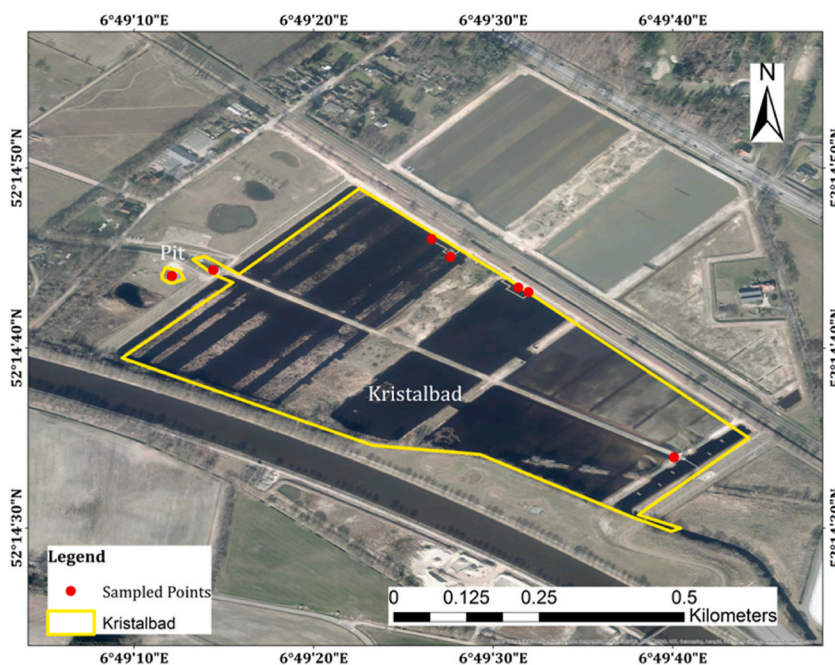


**Fig. 2.** Google Earth map showing Kristalbad artificial wetland (yellow boundary line) with overlaid sampled points (red dots). (For interpretation of the references to colour in this figure legend, the reader is referred to the Web version of this article.)

scattered clouds, fluctuating sunshine and relatively small wind (Markirzaatmeer Lake), no wind and about 60–90 % of cloud cover (Hulsbeek Lake), and clear sky, sunshine and gentle wind (Kristalbad artificial wetland). In all, 53 measurement sites were visited with distance ranging from 50 to 1000 m.

At each station, measurements carried out included; smartphone-captured images, hyperspectral sensors measurements, and water samples collected for laboratory analysis. The smartphone images for each site were taken using a Samsung Galaxy S4 GT-i9515 through the HydroColor APP. The images included; a grey card, water surface and sky image taken at zenith angle 37°–45°, 36°–46° and 120°–134° respectively. In two of the field campaigns (Binnenschelde and Hulsbeek), a printed grey paper was used in place of a grey card. Also, an Alcatel One Touch 7041D smartphone was used to take same measurement as the Samsung Galaxy S4 GT-i9515 as back up. However, the Alcatel One Touch 7041D smartphone images were not used in the analysis. The hyperspectral sensor measurements included; TriOS RAMSES-ACC-VIS irradiance sensor and TriOS RAMSES-ACC radiance sensor. The two sensors were first used to take measurements instantaneously for downwelling sun-sky irradiance and upwelling water radiance. For Markirzaatmeer Lake and Kristalbad artificial wetland, the TriOS RAMSES-ACC radiance sensor was later used to take the measurement for the sky radiance considering its fluctuation weather condition and sunny condition respectively. Water samples were also collected at randomly selected points corresponding to smartphone images in 2 L sampling bottles wrapped in aluminium foil to prevent light interaction with the water samples. To prevent degradation of the water samples, 3–6 drops of Magnesium Hydroxy Carbonate ( $4\text{MgCO}_3 \cdot \text{Mg}(\text{OH})_2 \cdot 5\text{H}_2\text{O}$ ) was added. The water samples were then refrigerated at 5 °C after which they were analysed for turbidity and [SPM]. Turbidimeter of model 2100P was used for measuring the turbidity of the water samples as described in the instrument manual of [9]. Using the gravimetric method as described in Ref. [10] the [SPM] were quantified. In-situ water quality variables of pH,

**Table 1**

Summary of the datasets, tools/protocols, and the quantity of information that was collected from a field campaign and laboratory analysis of water samples.

Data	Tool/Protocol	Quantity
Citclops	Samsung Galaxy S4 GT-i9515 and Alcatel One Touch 7041D.	sRGB of water surface images.
HydroColor	Samsung Galaxy S4 GT-i9515 and Alcatel One Touch 7041D.	sRGB images of water surface, sky, grey card, and printed grey paper (in place of the grey card when absent).
Hyperspectral sensors	TriOS RAMSES-ACC-VIS irradiance sensor.	Sky-sun downwelling irradiance.
Hyperspectral sensors	TriOS RAMSES-ACC radiance sensor.	Water leaving radiance.
In-situ water quality variables	HQ40d portable multimeter with two probes.	pH, dissolved oxygen, and temperature.
Water samples for laboratory analysis	Turbidimeter	Turbidity
Water samples for laboratory analysis	Gravimetric method	Concentration of suspended particulate materials [SPM]

dissolved oxygen and temperature were also measured using an HQ40d portable multimeter with two probes. A summary of the data sets of smartphone images, hyperspectral sensors, and water samples that were taken from the field campaigns for laboratory measurements are as shown in Table 1.

## 2.2. HydroColor APP data processing

Here below is an elaboration on the derivation of remote sensing reflectance of an RGB smartphone image  $R_{rs}(RGB)$  from the HydroColor APP of [7]. Point captured images of the grey card, sky and water surface were processed to derive the  $R_{rs}(RGB)$ . Each image was read in an array ranging from 0 to 255 and displayed. A displayed image was then cropped at the middle of the grey card and sky images. For a water surface image, an area with less specular reflectance, and no whitecaps was cropped. The RGB bands for each cropped image were then extracted using a MATLAB programme. The RGB intensity (grey level) values were then normalised from 0 to 1 and subsequently averaged to obtain single values for each band.

In the case of the printed grey paper, the derived RGB of these images had to be recalibrated to account for the printer tint on paper, that is, to account for the standard colour of the grey card. Following the same procedure, the RGB of 5 images of a grey card and 5 images of the printed grey paper all taken under shadowed condition were derived. A relation was then established between the grey card and printed grey paper using linear regression as shown in Eq. (1).

$$\text{Required grey card results} = (\text{printed paper} \times \text{slope}) + \text{intercept} \quad (1)$$

The linear regression coefficients as shown in Eq. (1) were then used to correct for the RGB of the printed grey paper images. The resulting RGB values of the required images were then used to obtain the relative radiance  $L_{rel}(RGB)$  of the images using Eq. (2). The camera's exposure time ( $\alpha$ ) during the capture of an image was obtained from the HydroColor APP Library of the smartphone.

$$L_{rel}(RGB) = \frac{RGB}{\alpha} \quad (2)$$

The remote sensing reflectance for each band  $R_{rs}(RGB)$  was then obtained using Eq. (3).

$$R_{rs}(RGB) = \frac{L_{rel}(L_{sfc}(RGB)) - \rho \times L_{rel}(L_{sky}(RGB))}{\frac{\pi}{R_{ref}} L_{rel}(L_{gc}(RGB))} \quad (3)$$

Where;  $L_{rel}(L_{sfc}(RGB))$  = the relative water surface radiance,  $L_{rel}(L_{sky}(RGB))$  = the relative sky radiance,  $L_{rel}(L_{gc}(RGB))$  = the relative grey card radiance,  $R_{ref}$  = the standard reference reflectance of the grey card which was taken as 0.18 and  $\rho$  = the sun-sky glint correction coefficient at the air-water interface taken as 0.028 from Ref. [11] as specified for the HydroColor APP.

The remote sensing reflectance of the red band,  $R_{rs}(R)$  derived from the smartphone images were used to then obtain estimates of turbidity and [SPM] using specific models used by the HydroColor APP. The model used to estimate turbidity ( $Turb$ ) from the  $R_{rs}(R)$  as cited in Ref. [7] is as shown in Eq. (4). From this model, 0.044 is the saturation of the red band reflectance ( $sr^{-1}$ ) and 22.57 is the estimate of turbidity (FTU, Formazine Turbidity Unit) for which the red band reflectance is at half the saturation level as defined by Ref. [12].

$$Turb = \frac{22.57 R_{rs}(R)}{0.044 - R_{rs}(R)} \quad (4)$$

The APP uses a relation of turbidity (in FTU) and the [SPM] to estimate  $\log_{10}[SPM]$  as cited in Ref. [7] and shown in Eq. (5); It should be noted that FTU is equivalent to NTU (Nephelometric Turbidity Unit).

$$\log_{10}[SPM] = 1.02 \log_{10}(Turb) - 0.04 \quad (5)$$

A detailed description of the models can be obtained from Ref. [7]. Laboratory results of turbidity and [SPM] for the corresponding sampled sites of the smartphone images were used to validate the HydroColor APP models. Parameters that were of interest were the coefficient of determination ( $R^2$ ), and the root mean square error (RMSE). The limitations of the models were then determined by varying the models' parameters, that is, their coefficients and the  $R_{rs}(R)$ .

The hyperspectral sensors measurements hereafter referred to as RAMSES were also used to derive their remote sensing reflectance  $R_{rs}(\lambda)$ . RAMSES data of  $R_{rs}(\lambda)$  were converted to  $R_{rs}(RGB)$  to make it comparable to the derived smartphone images  $R_{rs}(RGB)$ . Since the spectral response functions of the smartphone could not be obtained, the standard colourimetric 2-degree observation Colour Matching Functions, CMF's ( $\bar{x}$ ,  $\bar{y}$  and  $\bar{z}$ ) of CIE1931 were used. The CMF's of CIE1931 were downloaded from the Institute of Ophthalmology Colour and Vision Research Laboratory through the following link: <http://cvrl.ioo.ucl.ac.uk/cmfs.htm>. The derivation of the  $R_{rs}(\lambda)$  and the  $R_{rs}(RGB)$  of RAMSES is detailed in Ref. [13]. The  $R_{rs}(RGB)$  of RAMSES were then compared to the  $R_{rs}(RGB)$  of the smartphone images.

## 2.3. Citclops APP data processing

The RGB bands extracted from the cropped water surface images of Section 2.2 were used. Based on the Water Colour from Digital Images (WACODI) model of [14], gamma correction, chromaticity adaptation and illumination correction were applied to these images. The chromatically adapted image for each point measurement was then used to calculate the xyz chromaticity coordinates and



subsequently the  $\alpha_p(^{\circ})$  and FUI based on the Forel-Ule MERIS (FUME) model of [15]. Subsequently, the  $\alpha_p(^{\circ})$  derived from the smartphone images were compared to  $\alpha_N(^{\circ})$  of [16], obtained from laboratory prepared FU solutions transmission measurements of their experiment with the results shown in Fig. 3.

From the  $R_{rs}(\lambda)$  of RAMSES,  $\alpha_p(^{\circ})$  and FUI were derived by using the FUME model of [15] as applied to the smartphone images. The  $\alpha_p(^{\circ})$  and FUI of the smartphone images on comparison with the  $\alpha_p(^{\circ})$  and FUI derived from RAMSES were then used to calculate the deviation ( $\Delta$ ) of the smartphone images from RAMSES (which is considered to be the “true” measured colour of the water bodies). The  $\Delta$  of the smartphone images from RASMES were then used to develop a model for the smartphone images  $\alpha_p(^{\circ})$   $\Delta$  as applied on MERIS data by Ref. [17].

Visual judgement was also used to compare the smartphone water surface images to the RGB FU scale developed by Ref. [15]. This was by using the RGB values of the FU scale to generate images and their corresponding FUI to visually compare these images to the smartphone images.

The  $R_{rs}(\lambda)$  of RAMSES on converting to the xyz chromaticity coordinate were also compared to the xyz chromaticity coordinate of the smartphone images. First, the  $R_{rs}(\lambda)$  of RAMSES were normalised by dividing  $R_{rs}(\lambda)$  values for each wavelength by the maximum  $R_{rs}(\lambda)$  value. The normalised  $R_{rs}(\lambda)$  of RAMSES (as a colour function in the spectrum) were then multiplied by the standard colourimetric 2-degree CMF’s ( $\bar{x}$ ,  $\bar{y}$  and  $\bar{z}$ ) of CIE1931 and integrated over the visible spectrum (from 380 to 780 nm) following the Grassmann’s law in optics [18]. This resulted in single tristimulus values (X, Y and Z) computed for each  $R_{rs}(\lambda)$  spectral curve. Out of this, the xyz chromaticity coordinate were derived for RAMSES as detailed in Ref. [13]. A flow chat summarizing the study process for the data analysis is as shown in Fig. 4.

### 3. Results and discussions

#### 3.1. Field measurements

Results of selected smartphone water surface images that were used and subsequently processed according to Section 2.2 and 2.3 are as shown in Fig. 5a-e. This indicates the range of water systems that were used for the study; from blue-green to brown.

The resulting  $R_{rs}(\lambda)$  curves from the various study areas acquired through RAMSES are as shown in Fig. 6a-e. The  $R_{rs}(\lambda)$  curves of the point measurements are shown as blue lines whereas the coefficient of variation (CV) between the wavelengths is shown as a red line. The magnitude of variation of the  $R_{rs}(\lambda)$  across the spectral curves specifies the absorption and scattering of water molecules and the specific properties of each optically significant constituent and their effects on a light field as a function of wavelength. Of the water types studied, Hulsbeek Lake (a) showed the lowest CV (0.13) whiles Kristalbad artificial wetland (d) the highest CV (2.49).

#### 3.2. Comparison of RAMSES $R_{rs}(RGB)$ and smartphone images $R_{rs}(RGB)$

Using the three images (grey card, sky and water surface) of the smartphone, the  $R_{rs}(RGB)$  of each site was obtained as described in Section 2.2. The relations between the  $R_{rs}(RGB)$  derived from RAMSES data and  $R_{rs}(RGB)$  derived from the smartphone images are as shown in Fig. 7a and 7b respectively. It was observed that the  $R_{rs}(RGB)$  values obtained from RAMSES were higher than the  $R_{rs}(RGB)$  obtained from the smartphone images. The maximum absolute variation between RAMSES  $R_{rs}(RGB)$  and the smartphone images  $R_{rs}(RGB)$  were obtained to be 0.022, 0.020 and 0.016 for the R, G and B bands. The resulting relations from this analysis were not good with percentage error PE of 69 %, 67 % and 77 % for the R, G and B bands respectively. The  $R^2$  on the other hand was 0.22, 0.21 and 0.32 for R, G and B bands respectively. With the  $R_{rs}(RGB)$  of the smartphone images, any scaling error from the smartphone camera would have been cancelled from the subtraction and division of the three images used in calculating the  $R_{rs}(RGB)$  of the water surface

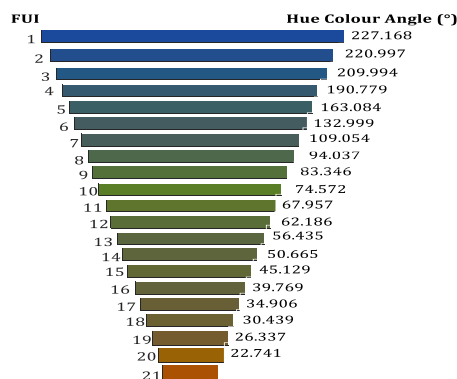


Fig. 3. Hue colour angles  $\alpha_N(^{\circ})$  and their corresponding Forel-Ule Index (FU 1 to 21) of [16]. These  $\alpha_N(^{\circ})$  were derived from laboratory FU solutions of transmission measurements of their research. The Figure was developed using RGB colour values for the reproduction of the FU legend by Ref. [15]. (For interpretation of the references to colour in this figure legend, the reader is referred to the Web version of this article.)

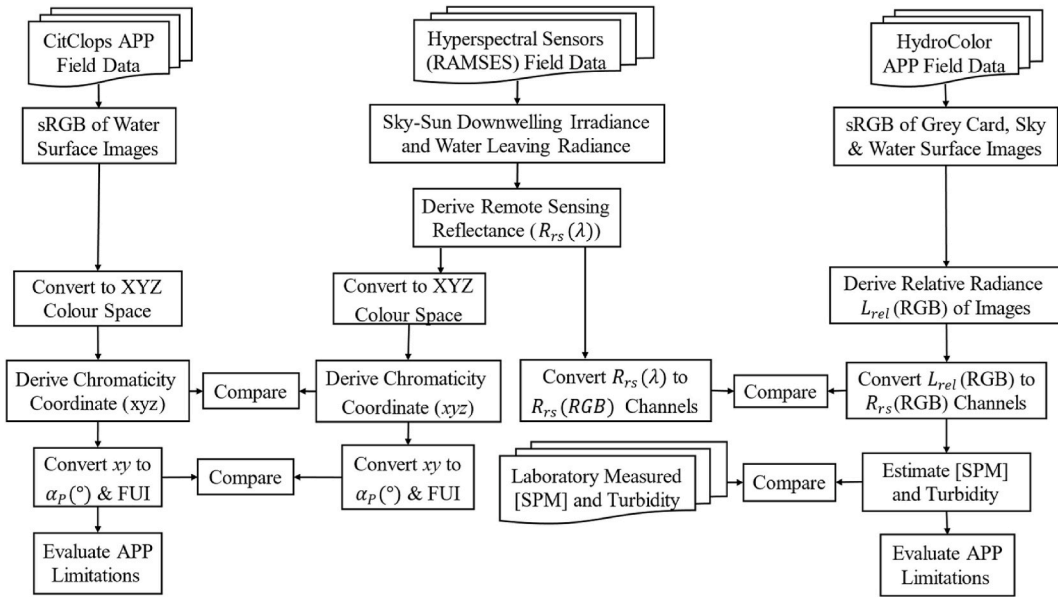


Fig. 4. Flow chat summarizing the study process.

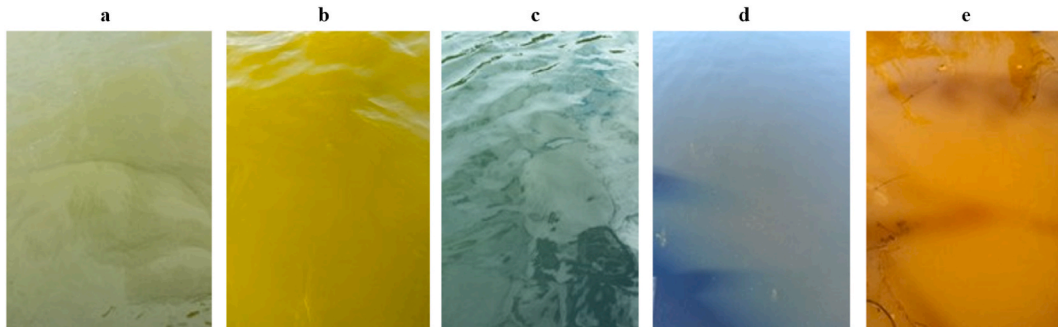
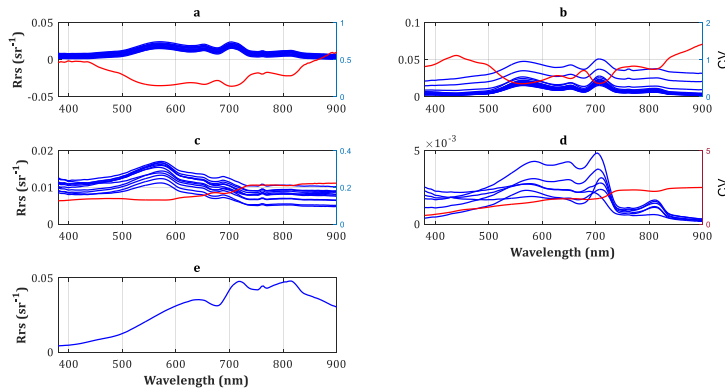


Fig. 5. Selected smartphone water surface images of the studied surface water systems. From left to right; Binnenschelde Lake (a), Markiezaatsmeer Lake (b), Hulsbeek Lake (c), Kristalbad artificial wetland (d), and a pit water at the Kristalbad artificial wetland (e).

[7]. Thus, the primary source of error associated with the results was due to the convolution of the 2-degree field of view CMFs of CIE1931 with RAMSES  $R_{rs}(\lambda)$  instead of the spectral response functions of the smartphone device used. The results obtained indicated that, the CIE1931 CMFs cannot be recommended as use in place of the spectral response function of a smartphone. First,  $R_{rs}(RGB)$  is of the RGB colour space and depends on the sensitivity function of the device used. Thus, to make the result of the smartphone  $R_{rs}(RGB)$  comparable to the  $R_{rs}(RGB)$  of RAMSES, the convolution of RAMSES should have been done with the smartphone’s spectral response. Secondly, the CMFs of the CIE1931 are illumination independent and are, thus, theoretical representation of the spectral response.

### 3.3. Comparison of RAMSES xyz and smartphone images xyz

The correlation of RAMSES xyz chromaticity coordinates and the smartphone images xyz chromaticity coordinates are as shown in Fig. 8a and 8b respectively. The xyz chromaticity coordinates of RAMSES and the smartphone images showed a correlative pattern for the sample sites as shown on the left panel of the Figure. The maximum absolute variation between the two devices were obtained to be 0.101, 0.058 and 0.159 for x, y and z respectively. The results of the correlation also indicated the highest value(s) of; x chromaticity coordinate at the CDOM dominated water site, y chromaticity coordinate for chlorophyll-a pigment dominated water sites and z chromaticity coordinate at the clear water sites. Scatter plots of the xyz chromaticity coordinates of RAMSES and the smartphone images are as shown on the right panel of Fig. 8. The Figure indicates a correlation of  $R^2$  0.65, 0.70 and 0.67 respectively for x, y and z. the PE were also 9.69 %, 0.07 % and 22 % respectively for x, y and z.



**Fig. 6.** Spectral reflectance curves  $R_{rs}(\lambda)$  (blue lines) for the sample sites and their corresponding coefficient of variation (CV) of the wavelengths (red line). For all the measurements [11] sun-sky glint correction factor of 0.028 was used to correct for specular reflectance except for Hulsbeek Lake (c). (a) Binnenschelde Lake; (b) Markiezaatsmeer Lake; (c) Hulsbeek Lake; (d) Kristalbad Artificial Wetland; (e) CDOM dominated pit water sampled near Kristalbad artificial wetland. (For interpretation of the references to colour in this figure legend, the reader is referred to the Web version of this article.)

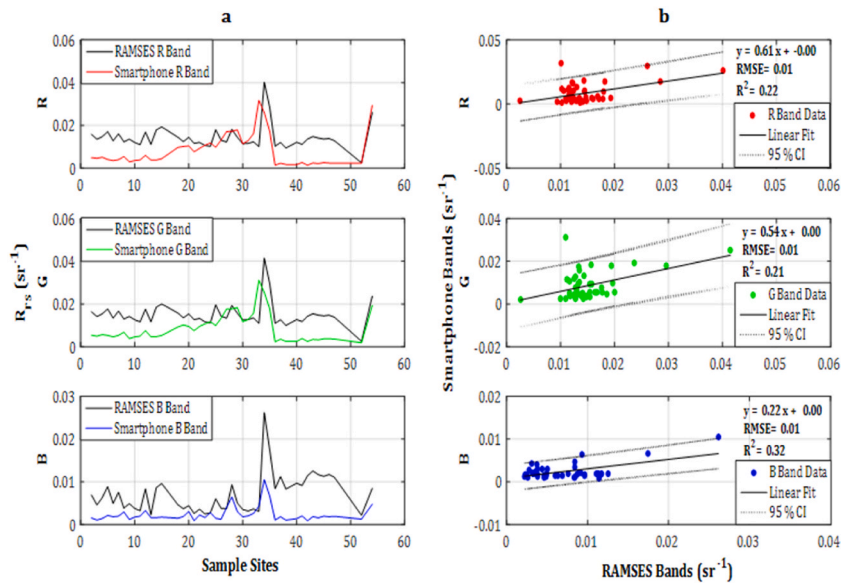


**Fig. 7.** The relationship between derived RAMSES  $R_{rs}(RGB)$  and smartphone images  $R_{rs}(RGB)$  of the studied water bodies. (a) The variation of RAMSES and smartphone images  $R_{rs}(RGB)$  with respect to sample sites. (b) The correlation between RAMSES  $R_{rs}(RGB)$  versus smartphone images  $R_{rs}(RGB)$ .

### 3.4. Laboratory measurements

Results of the laboratory measurements of the water samples for turbidity and [SPM] with their sampled sites are shown as bar plots of Fig. 9a and 9b respectively. Measurements for turbidity ranged from 1.4 to 163.4 NTU. The measurements for [SPM] ranged from 7.6 to 136.0  $\text{gm}^{-3}$ . The results indicated a wide variation of the water type sampled with two orders of magnitude for both turbidity and [SPM]. However, turbidity showed the highest variation with 1.65 as the CV compared to 0.75 of the [SPM]. The relation between turbidity and [SPM] was found to be 1 NTU: 4  $\text{gm}^{-3}$  after removing the extreme turbidity sample point. The correlation between turbidity and [SPM] after removing the extreme turbidity sample point also indicated an  $R^2$  of 0.79. The significant relation between turbidity and [SPM] confirmed the direct relation of these two variables stated in literature [19–21]. According to Ref. [22] where a linear model was developed for this two water quality variables, the relation work for both Case 1 and Case 2 water.

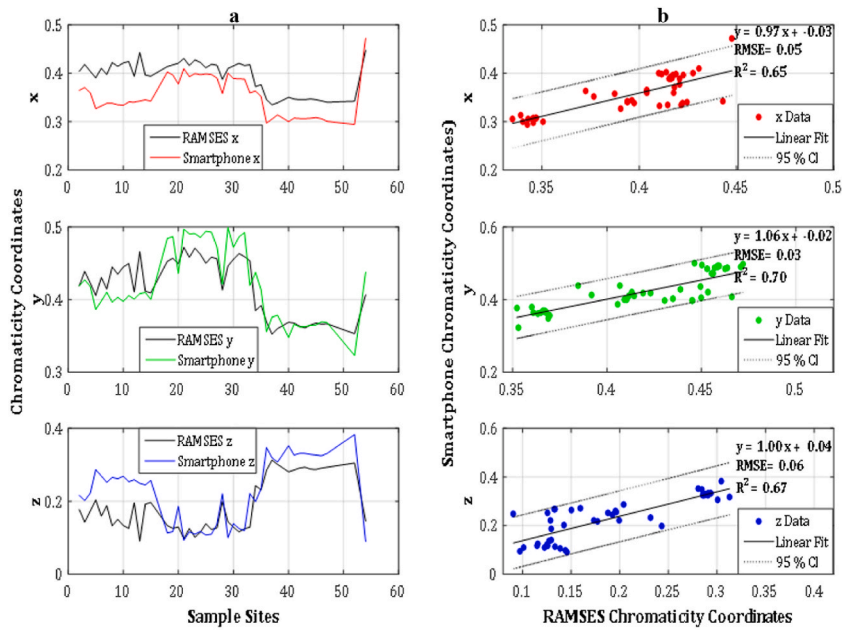


**Fig. 8.** Relationship between RAMSES xyz chromaticity coordinates and smartphone images xyz chromaticity coordinates. The x data is specified by red, y data by green and the z data by blue. The left panel of the figure, (a) indicates the plot of the xyz chromaticity coordinates versus the sample sites. On the right panel, (b) are the scatter plots of the xyz chromaticity coordinates of RAMSES versus the smartphone images. (For interpretation of the references to colour in this figure legend, the reader is referred to the Web version of this article.)

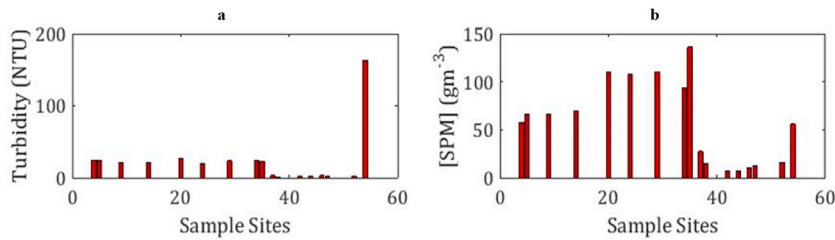


**Fig. 9.** Bar plots of laboratory measured water quality variables with respect to their sample sites. (a) Turbidity (NTU). (b) [SPM] ( $\text{gm}^{-3}$ ), the concentration of suspended particulate materials.

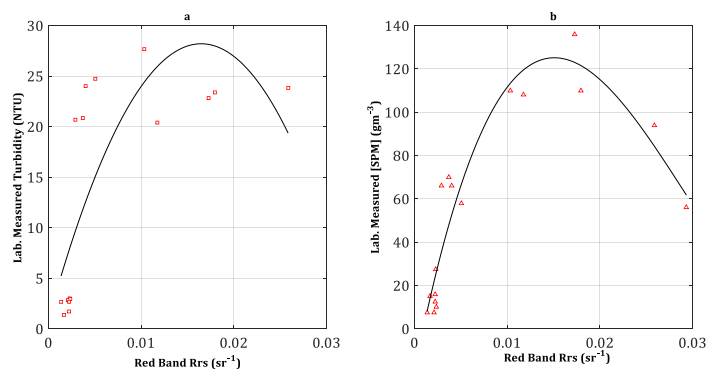


**Fig. 10.** The relationship between laboratory measured turbidity and the [SPM], and the red band reflectance of the smartphone images. (a) Smartphone images red band reflectance versus lab measured turbidity. (b) Smartphone images red band reflectance versus lab measured [SPM]. (For interpretation of the references to colour in this figure legend, the reader is referred to the Web version of this article.)



### 3.5. HydroColor APP water quality variables

The relation between the laboratory measured turbidity and [SPM], and the red band reflectance  $R_{rs}(R)$  of the smartphone images was determined by fitting two and three-degree polynomial respectively as shown in Fig. 10a and 10b. For turbidity, the relation indicated an RMSE of 7.32 NTU with  $R^2$  of 0.60. The relation for [SPM] also gave an RMSE of 15.08  $\text{gm}^{-3}$  and  $R^2$  of 0.89. Therefore, it was observed that turbidity and [SPM] influence the reflectance of the water bodies in the red band of the smartphone images. However, for the datasets used for this study, the relation only holds for turbidity less than 28 NTU with a reflectance of 0.0165  $\text{sr}^{-1}$  and [SPM] less than 128  $\text{gm}^{-3}$  with reflectance of 0.015  $\text{sr}^{-1}$ . The reflectance in the red band increased with increase in turbidity up to approximately 20 NTU before it turns to saturate. A similar (but not identical) dependence of turbidity and the red band reflectance was observed using iPod Touch, iPhone 4 and iPhone 5 devices with the HydroColor APP by Ref. [7] and also for the red band wavelength 645 nm of a multispectral sensor product used by Ref. [23] in their research.

The lower correlation of the reflectance in the red band with turbidity than with [SPM] might be attributed to differences in particle size distribution within the water bodies [22]. This is because; the turbidity meter uses the amount of backscattered light in its computation. For instance Ref. [24], reported that homogeneous spherical particles smaller than 2.4  $\mu\text{m}$ , contribute more to backscattering of water as they scatter light in equal intensities in all directions. Also, studies indicate that particles larger than 302  $\mu\text{m}$  may contribute more backscattering of water as particles larger than the wavelength of the light source used by the turbidimeter results in greater forward scattering [25]. In this case, such an effect was likely to have been encountered for homogeneously smaller particle size and larger particle size in the water samples used for the laboratory measurements. The results also indicated that in some case, as turbidity increased the reflected light in the red band decreased as observed in Fig. 10 a. Research conducted by Ref. [26] indicated that as particle scattering decrease with increase in the [SPM] of homogeneously smaller particle size and of larger particle size, this causes a reduction in the water surface reflectance.

Using the relation of the red band reflectance to turbidity and [SPM] as shown in Eqs. (4) and (5), estimations of these water quality variables were obtained as specified for the HydroColor APP. Results of validation of the APPs models with the laboratory measurements is as shown in Fig. 11a and 11b for turbidity and [SPM] respectively. The results indicated a good correlation of  $R^2 = 0.68$  and RMSE = 7.37 NTU for turbidity. The [SPM], on the other hand, gave a correlation of  $R^2 = 0.38$  and RMSE = 10.75  $\text{gm}^{-3}$ . It should, however, be noted that these results were based on using all the corresponding laboratory measurements of the smartphone images' red band reflectance.

Based on the previous relation of the reflectance in the red band with turbidity and [SPM], reflectance values  $> 0.02 \text{sr}^{-1}$  were excluded from the data since the water quality variables estimates above this reflectance were considered not reliable. The relation between the laboratory measurements and the estimated smartphone images results were again determined. The results from this relation as shown in Fig. 12a and 12b gave  $R^2 = 0.36$  and RMSE = 4.13 NTU for turbidity while  $R^2 = 0.83$  and RMSE = 3.44  $\text{gm}^{-3}$  for [SPM] respectively. This indicated a decrease in the correlation between turbidity and an increase for [SPM] as compared to results of all the reflectance values of Fig. 11a and 11b respectively.

### 3.6. Limitations of HydroColor APP

The limit of the models used to estimate turbidity and [SPM] by the HydroColor APP were evaluated by varying the red band reflectance. From the turbidity model of Eq. (4), the saturation of the red band reflectance occurs at 0.044  $\text{sr}^{-1}$  and the concentration of turbidity at half the saturation was 22.57 NTU. From the results obtained as shown in Fig. 13a, the estimate of turbidity starts at 0 NTU when the red band reflectance = 0  $\text{sr}^{-1}$ . As turbidity gets larger the red band reflectance approaches an asymptote at 0.044  $\text{sr}^{-1}$ . The

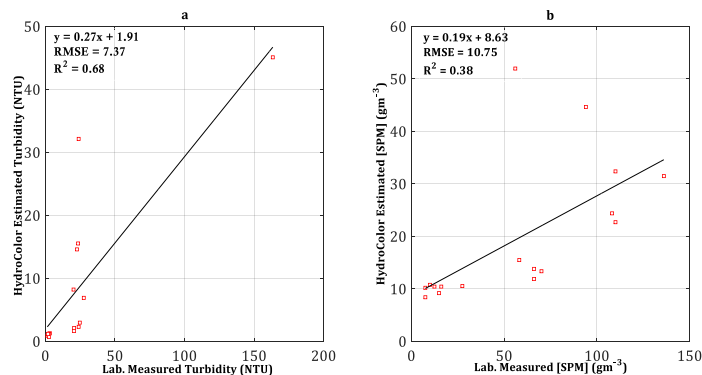


**Fig. 11.** Validation of the specified models used by HydroColor APP to estimate turbidity and the [SPM]. (a) Estimates of turbidity through the semi-analytical model of the HydroColor APP versus laboratory measured turbidity. (b) Estimates of the [SPM] through the logarithmic model of HydroColor APP versus laboratory measured [SPM]. The relations were based on all the corresponding red band reflectance of the smartphone images to laboratory measurements. (For interpretation of the references to colour in this figure legend, the reader is referred to the Web version of this article.)

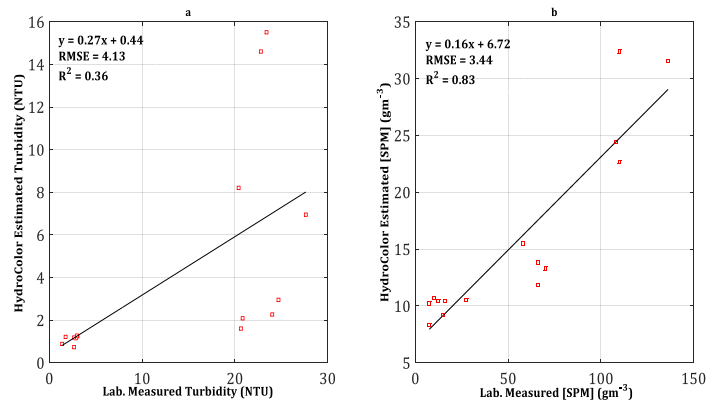


**Fig. 12.** Validation of the specified models used by HydroColor APP to estimate turbidity and [SPM]. (a) Estimates of turbidity through the semi-analytical model of HydroColor APP versus laboratory measured turbidity. (b) Estimates of the [SPM] through the logarithmic model of HydroColor APP versus laboratory measured [SPM]. The relations were based on measurements of the red band reflectance of the smartphone images  $<0.02 \text{ sr}^{-1}$ . (For interpretation of the references to colour in this figure legend, the reader is referred to the Web version of this article.)

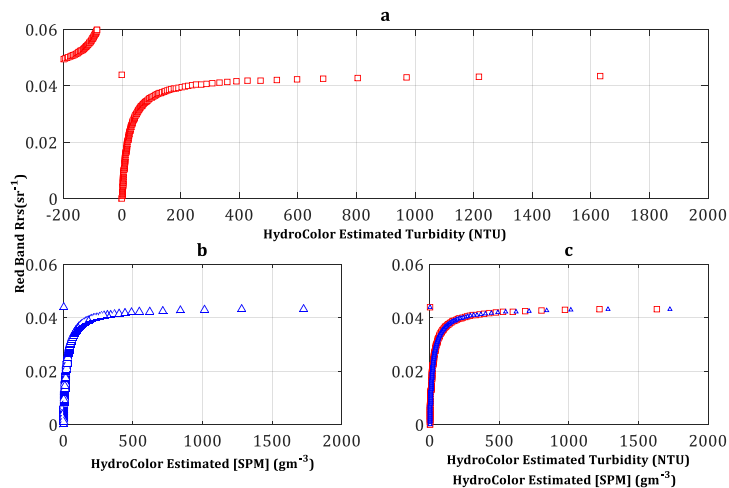


**Fig. 13.** Simulation of the estimation of turbidity and [SPM] from the red band reflectance to determine the limitations of the models used by HydroColor APP. (a) Estimated turbidity versus the red band reflectance. (b) Estimated [SPM] versus the red band reflectance. (c) The 1 NTU: 1  $\text{gm}^{-3}$  relation of turbidity and [SPM] applied by HydroColor APP showing an overlap of the two estimated water quality variables. (For interpretation of the references to colour in this figure legend, the reader is referred to the Web version of this article.)

limit of turbidity estimate before the asymptote is approximately 4943 NTU. As can be seen from the Figure, the major limitation to this model is that reflectance values above the saturation limit of  $0.044 \text{ sr}^{-1}$  give negative turbidity results. With the possibility of having to encounter a water system with reflectance  $\geq 0.044 \text{ sr}^{-1}$  which is typical of very turbid water dominated with colour dissolved organic materials (CDOM) or suspended mineral substance [27], this model would not be able to estimate the concentration of turbidity in such case. On a positive note, the results indicated that the model would give an estimate of turbidity and [SPM] no matter how small the optical signal received by the smartphone may be. For instance, the estimate of turbidity and [SPM] at a reflectance value of  $0.0001 \text{ sr}^{-1}$  gave  $0.05 \text{ NTU}$  and  $0.04 \text{ gm}^{-3}$  respectively. Thus, the HydroColor APP can be used on optically clear water systems.

In the same contest, since [SPM] is estimated from the concentration of turbidity as derived in Eq. (5) the estimation of [SPM] will fall under the same limitation. Thus, as shown in Fig. 13a for turbidity, a similar result was obtained for [SPM] as shown in Fig. 13b. This is because, the HydroColor APP model for turbidity and [SPM] has approximately 1 NTU: 1  $\text{gm}^{-3}$  relation based on researches conducted by Refs. [22,28] as cited in Ref. [7]. Therefore, this would give the results for these water quality variables to approximately overlap as observed in Fig. 13c. The limit of the [SPM] estimate before the asymptote specified for the HydroColor APP was, therefore, obtained to be approximately  $5344 \text{ gm}^{-3}$ . From the laboratory measurements indicated previously, the relation between turbidity and [SPM] was observed to be approximately 1 NTU:  $4 \text{ gm}^{-3}$ . In this case, the model used by HydroColor APP would underestimate the [SPM] of the water bodies studied.

### 3.7. Citclops APP water quality variable

An illustration of selected xy chromaticity coordinates of RAMSES and the smartphone images are as shown in a chromaticity diagram of Fig. 14. The Figure indicates the derived chromaticity coordinates of the devices with respect to the chromaticity coordinates that were developed from laboratory FU solution transmission measurements by Ref. [16]. It was observed that the chromaticity coordinates of RAMSES were closer to the white point (WP) as compared to the smartphone images chromaticity coordinates. The closeness of RAMSES chromaticity coordinates to the WP indicated that its resulting colours were less saturated as compared to the smartphone images. This could be as a result of the gamma expansion that was applied on the smartphone images as specified for the WACODI model [14]. By gamma expansion with a value of 2.2 which is specified for the WACODI model, the colour of the output smartphone images became saturated with the enhancement of their grey level.

Statistical summary of the  $\alpha_p(^{\circ})$  and FUI that were derived from RAMSES and the smartphone images are as follows. The  $\alpha_p(^{\circ})$  derived from RAMSES data ranged from 32.68 $^{\circ}$  to 85.47 $^{\circ}$  and FUI ranged from 9 to 18. The  $\alpha_p(^{\circ})$  of the smartphone images ranged from 36.90 $^{\circ}$  to 156.85 $^{\circ}$  and FUI ranged from 6 to 17. Comparison of the  $\alpha_p(^{\circ})$  and FUI derived from RAMSES and the smartphone images are as shown in Fig. 15a and 15b respectively. With the  $\alpha_p(^{\circ})$ , the  $R^2$  obtained was 0.63 and an RMSE of 17.20 $^{\circ}$ . Fig. 15 also indicated that the  $\alpha_p(^{\circ})$  of the data set within the third quartile were more dispersed. This could be due to the high angular differences existing in the blue to cyan hue colour angles as can be seen in Fig. 3. Quite apart, the water system that was characterised by these angles was the clear water body of Hulsbeek Lake with measurements taken under fluctuating weather condition. The effect of such fluctuating weather condition could have also caused a significant influence on the water surface reflectance which in this case resulted in varying angles. For the FUI, the correlation between RAMSES and the smartphone images gave  $R^2$  of 0.70 and RMSE of 1.32. The consistency in the FU 14 for the RAMSES data was for Binnenschelde and Markiezaatsmeer Lake which had similar water characteristics. It was therefore expected to have the same range of FUI as was observed from RAMSES (considered to be the “true” results).

### 3.8. Limitations of citclops APP

Variations in  $\alpha_p(^{\circ})$  as seen from Fig. 15 caused significantly the derived FUI. To identify such areas of  $\alpha_p(^{\circ})$ , the  $\Delta$  of the smartphone images from RAMSES (considered to be the “true” measurements) were determined. This was by subtracting the  $\alpha_p(^{\circ})$  of the smartphone images from RAMSES  $\alpha_p(^{\circ})$ . The derived  $\Delta$  of  $\alpha_p(^{\circ})$  with respect to the sample sites are as shown in Fig. 16a. It was observed that there was much variation in the sample sites of Hulsbeek Lake up to  $-92.71^{\circ}$ .

Next, Fig. 16b indicates that the smartphone images with  $\alpha_p(^{\circ}) > 100^{\circ}$  gave most of its deviation  $< -50^{\circ}$ . From Fig. 3,  $\alpha_p(^{\circ}) > 100^{\circ}$  correspond to FU 7 to 1. It was this observed that FUI derived with  $\alpha_p(^{\circ}) > 100^{\circ}$  gave much variation in FUI as shown in Fig. 16c. Such disparity in  $\alpha_p(^{\circ})$  which subsequently affected the FUI of Hulsbeek Lake could be attributed to its clear water system (of  $\alpha_p(^{\circ}) > 100^{\circ}$ ) and fluctuation in weather condition. Also, its RAMSES  $R_{rs}(\lambda)$  were not corrected for sky glint effects which could contribute to such deviation because of the clear start of the water at the time the study was conducted.

The Hulsbeek’s Lake results were thus removed from the data set and the remaining  $\alpha_p(^{\circ})$  used to develop a model on which  $\Delta$  of the smartphone images  $\alpha_p(^{\circ})$  from the “true”  $\alpha_p(^{\circ})$  of RAMSES was obtained. This was by fitting a three-degree polynomial function to the data set. The results obtained indicated a good fit with an  $R^2$  of 0.97 and RMSE of 2.00 $^{\circ}$  as shown in Fig. 16d with the resulting model shown in Eq. (6).

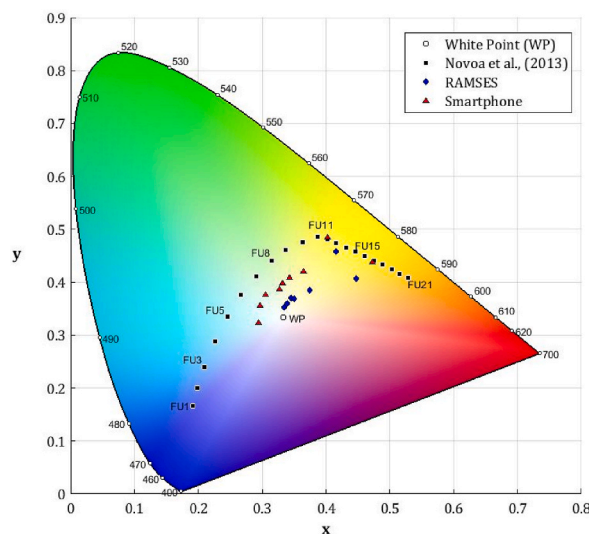
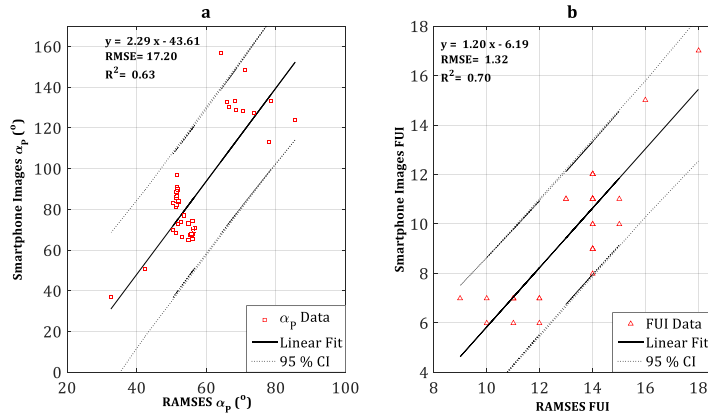
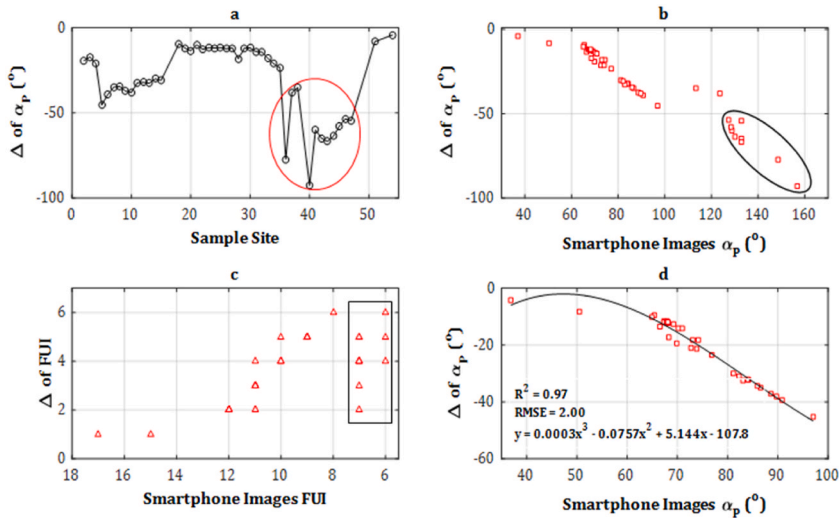


Fig. 14. Illustration of the xy chromaticity coordinates derived from RAMSES and the smartphone images on a chromaticity diagram. This is compared to the chromaticity coordinates that were developed from laboratory FU solution transmission measurements by Ref. [16]. The white point of the chromaticity coordinate is indicated as WP.



**Fig. 15.** Relationship between the hue colour angle  $\alpha_P(^{\circ})$  and Forel-Ule Index (FUI) derived from RAMSES and the smartphone images. (a) Scatter plot of the  $\alpha_P(^{\circ})$  derived from RAMSES and the smartphone images with a linear fit (full line) and the 95 % confidence interval (dotted lines). (b) Scatter plot of the FUI derived from RAMSES and the smartphone images with a linear fit (full line) and the 95 % confidence interval (dotted lines). (For interpretation of the references to colour in this figure legend, the reader is referred to the Web version of this article.)



**Fig. 16.** Deviation  $\Delta$  of the smartphone images hue colour angles  $\alpha_P(^{\circ})$  and Forel-Ule Index (FUI) from RAMSES. (a) Derived  $\Delta$  of the smartphone images  $\alpha_P(^{\circ})$  with respect to sample sites. (b) Derived  $\Delta$  of the smartphone images  $\alpha_P(^{\circ})$  with respect to the original  $\alpha_P(^{\circ})$  of the smartphone images. (c) Derived  $\Delta$  of the smartphone images FUI with respect to the original FUI of the smartphone images. (d) Derived  $\Delta$  of the smartphone images  $\alpha_P(^{\circ})$  for the sample sites excluding Hulsbeek Lake (36–47) in order to derive a model to correct for the  $\Delta$  of the smartphone images. (For interpretation of the references to colour in this figure legend, the reader is referred to the Web version of this article.)








$$\Delta_{\alpha_P}(^{\circ}) = 0.0003x^3 - 0.0757x^2 + 5.144x - 107.8 \tag{6}$$

It should, however, be noted that this hue colour angle deviation factor,  $\Delta_{\alpha_P}(^{\circ})$  cannot be applied on;  $36.896^{\circ} < \alpha_P(^{\circ}) > 99.991^{\circ}$ . Thus,  $\alpha_P(^{\circ})$  derived outside this interval with the addition of the  $\Delta_{\alpha_P}(^{\circ})$  will give inaccurate results.

Another comparison was to match the water surface images with the FU scale developed using RGB values by Ref. [15]. This was by using the RGB values of the FU scale to generate RGB colour images and their corresponding FUI. The resulting images were visually compared to the smartphone images. The results were relatively good for the smartphone images except for the pit water surface image of Fig. 4. From visual inspection, this water should correspond to FU 20–21 as can be visualised from the images in Fig. 3 and Table 2. Comparing the derived  $\alpha_P(^{\circ})$  of that point’s measurements to the  $\alpha_N(^{\circ})$  of [16], FU 17 was obtained for the smartphone image and FU 18 for RAMSES. However, the  $\alpha_P(^{\circ})$  of the smartphone image and RAMSES on relating to the  $\alpha_W(^{\circ})$  of [15] gave FU 21 for both devices. From the preliminary results displayed by Citclops APP when an image is first captured and sent to the Citclops database for subsequent processing, one could say the pit water contains extreme concentrations of humic acid which cover an FU range of 18–21 (check details from; <http://www.citclops.eu>). By this, the derived FUI of RAMSES and perhaps the smartphone image fall within the same range of water system for the  $\alpha_P(^{\circ})$  compared to the  $\alpha_N(^{\circ})$  of [16]. On the other hand, the “true” colour of the water translated to FUI would be

**Table 2**

Visual comparison of the pit water smartphone image  $\alpha_P(^{\circ})$  and FUI to the  $\alpha_W(^{\circ})$  and FUI generated using RGB values of [15] and the  $\alpha_N(^{\circ})$  and FUI of laboratory FU solution transmission by Ref. [16]. The FUI is calculated based on the  $\alpha_P(^{\circ})$ . For example, the  $\alpha_P(^{\circ})$  of the pit water smartphone image was 36.896°. Base on [16], this angle is < 39.769°. The smartphone image is thus indexed 17. Also, based on [15], this angle is < 39.674°. The point measured RAMSES data is thus indexed 21.

Water Surface Image	RGB Colour Images of FUI	Field Data	$\alpha_P(^{\circ})$	Novoa et al. (2013)		Wernand et al. (2013)	
				$\alpha_N(^{\circ})$	FUI	$\alpha_W(^{\circ})$	FUI
		RAMSES	32.677	39.769	16	58.623	16
				34.906	17	54.649	17
				30.439	18	49.527	18
		Smartphone Image	36.896	26.337	19	43.963	18
				22.741	20	39.674	20
				<22.741	21	<39.674	21

missed if the relation is based on the  $\alpha_P(^{\circ})$  to the  $\alpha_N(^{\circ})$  of [16]. Thus, the Citclops APP would underestimate the “true” colour of very turbid water bodies if the Citclops APP model is based on comparing smartphone images  $\alpha_P(^{\circ})$  with the  $\alpha_N(^{\circ})$  of [16]. However, a comparison of the point measured  $\alpha_P(^{\circ})$  to the  $\alpha_W(^{\circ})$  of [15] gave an accurate result.

#### 4. Conclusions

The capability of smartphones through APPs to quantify water quality variables such as turbidity, ([SPM]), and colour have been the subject of assessment for this research. This was accomplished by evaluating two existing smartphone APPs: HydroColor and Citclops. The HydroColor and Citclops APPs both use the RGB channels of a water surface image captured by a smartphone camera. However, they use different transfer functions (colour space) to estimate water quality variables from the smartphone image(s). The results of their transfer functions (that is, the  $R_{rs}(RGB)$  and the  $xyz$  chromaticity coordinates respectively of HydroColor and Citclops APP) derived from smartphone images on comparison with RAMSES cannot be conclusive. This is because, the  $R_{rs}(RGB)$  of RAMSES data was not weighed with the spectral response function of the smartphone. Thus, the correlation of smartphone images and RAMSES  $R_{rs}(RGB)$  were lower with  $R^2 \leq 0.32$ . The correlation of smartphone images and RAMSES  $xyz$  chromaticity coordinates on the other hand was good with  $R^2 \geq 0.65$ .

For the estimated water quality variables, the models used by the HydroColor APP in estimating turbidity and [SPM] after correlation with laboratory measurements indicated an  $R^2$  of 0.36 and 0.83 respectively. These models although averagely gave good results have  $R_{rs}(R)$  of 0.044  $sr^{-1}$  as the reflectance saturation limit thereby limiting the range of water type that can be studied with it. Therefore, the models will work well for optically clear water systems but will fail with very turbid or CDOM-dominated water systems. The study also indicated that the 1 NTU: 1  $gm^{-3}$  proximity relation of turbidity and [SPM] used by the HydroColor APP is not representative of all water bodies. The relation that was obtained for the water bodies used for this study was 1 NTU: 4  $gm^{-3}$ . For the Citclops APP, the resulting water colour of the smartphone images as the  $\alpha_P(^{\circ})$  translated into FUI gave a good correlation with RAMSES with  $R^2$  of 0.63 and 0.70 respectively. Since the study was limited by the data set, the model developed to correct for the offset in  $\alpha_P(^{\circ})$  was derived for  $\alpha_P(^{\circ})$  within 36.896° and 99.991°. After visual assessment of a pit water surface image against derived RGB colour images of the FU, it was observed that the  $\alpha_W(^{\circ})$  used by Ref. [15] with FU 21 gave a “true” colour of the water compared to  $\alpha_N(^{\circ})$  of [16] of FU 17.

Despite these advancements, it is evident that both APPs require proper calibration and validation to extend their utility across a wider range of water systems. Future research should focus on refining the models used by these APPs to improve accuracy and reliability, thereby enhancing their effectiveness in water quality monitoring. Overall, this study underscored the importance of ongoing efforts to advance smartphone-based monitoring technologies and their potential to revolutionize environmental monitoring practices. By leveraging the potential of smartphone technology, we can achieve more comprehensive and sustainable management of water resources, ultimately benefiting both ecosystems and human communities.



## Data availability

Data will be made available on request.

## CRediT authorship contribution statement

**Peter N-jonaam Mahama:** Writing – original draft, Visualization, Methodology, Formal analysis, Data curation. **Suhyb Mohammed Salama:** Validation, Supervision, Methodology, Conceptualization.

## Declaration of competing interest

The authors declare that they have no known competing financial interests or personal relationships that could have appeared to influence the work reported in this paper.

## Acknowledgements

The authors are grateful to the Department of Water Resources and Environmental Management of the Faculty of Geo-Information Science and Earth Observation (ITC) of the University of Twente. We would also like to thank the Vechtstromen and Brabantsedelta Water Boards for their supports. In particular we thank Arjan Segeren, Guido Waajen from the Brabantsedelta, Sjon Monnix and Leontien van der Molen from Vechtstromen and Bas Waanders, Park manager of Het Hulsbeek for providing the sampling boats and facilitating the field works. We further want to thank Justin Yieri, Christian Kwasi Owusu and Mujeeb Rahman Nuhu for their support during the data collection. Also, our profound gratitude to Dr. Shungu P. Garaba of the Marine Science Department of the University of Oldenburg for the MATLAB codes to derive FUI. Not to forget Mrs. Irina Miranda Miguel for the Alcatel One Touch 7041D smartphone for this research work.

## Abbreviations

*The following abbreviations are used in this manuscript*

APP	Application
CDOM	Colour Dissolved Organic Materials
CV	Coefficient of Variation
FUI	Forel-Ule Index
FUME	Forel-Ule MERIS
Lab	Laboratory
MATLAB	Matrix Laboratory
MERIS	Medium Resolution Imaging Spectrometer
NTU	Nephelometric Turbidity Unit
RAMSES	Radiation Measurement Sensor with Enhanced Spectral Resolution
RGB	Red, Green and Blue channels of an image
RMSE	Root Mean Square Error
R <sup>2</sup>	Determination Coefficient
[SPM]	Concentration of Suspended Particulate Materials
USD	United States Dollar
WACODI	Water Colour from Digital Images
WP	White Point

## References

- [1] Research and Markets, Global environmental sensing and monitoring technology analysis report 2023: market to reach \$19.3 billion by 2030 from \$14 billion in 2022 - environment sensing and monitoring to emerge as mainstream, Dublin, <https://www.globenewswire.com/en/news-release/2023/04/24/2653223/28124/en/Global-Environmental-Sensing-and-Monitoring-Technology-Analysis-Report-2023-Market-to-Reach-19-3-Billion-by-2030-from-14-Billion-in-2022-Environment-Sensing-and-Monitoring-to-Emerge.html>, 2023.
- [2] P. Corke, T. Wark, R. Jurdak, W. Hu, P. Valencia, D. Moore, Environmental wireless sensor networks, *Proc. IEEE* 98 (11) (2010) 1903–1917, <https://doi.org/10.1109/JPROC.2010.2068530>.
- [3] Q. Cao, G. Yu, Z. Qiao, Application and recent progress of inland water monitoring using remote sensing techniques, *Environ. Monit. Assess.* 195 (125) (2023) 1–16, <https://doi.org/10.1007/s10661-022-10690-9>.
- [4] S.P. Mertikas, P. Partsinevelos, C. Mavrocordatos, N.A. Maximenko, Environmental applications of remote sensing, in: S.P. Mertikas (Ed.), *Pollution Assessment for Sustainable Practices in Applied Sciences and Engineering*, Elsevier Inc., 2020, pp. 107–163, <https://doi.org/10.1016/B978-0-12-809582-9.00003-7>.
- [5] J.G. Arango, R.W. Nairn, Prediction of optical and non-optical water quality parameters in oligotrophic and eutrophic aquatic systems using a small unmanned aerial system, *Drones* 4 (1) (2020) 1–21, <https://doi.org/10.3390/drones4010001>.
- [6] M. Gao, et al., Smartphone-camera-based water reflectance measurement and typical water quality parameter inversion, *Rem. Sens.* 14 (6) (2022), <https://doi.org/10.3390/rs14061371>.

- [7] T. Leeuw, Crowdsourcing Water Quality Data Using the iPhone Camera, University of Maine, 2014.
- [8] S. Novoa, M.R. Wernand, H.J. van der Woerd, The Forel-Ule Scale Converted to Modern Tools for Participatory Water Quality Monitoring, 2014, <https://doi.org/10.13140/2.1.4179.4246>.
- [9] Hach, Portable Turbidimeter Model 2100P: Instrument and Procedure Manual, 2008.
- [10] G.H. Tilstone, et al., Regional validation of MERIS chlorophyll products in north sea REVAMP protocols regional validation of MERIS chlorophyll products in, *Work. Meet. MERIS AATSR Calibration Geophys. Valid. (ENVISAT MAVT-2003)* (2003) 1–77. October.
- [11] C.D. Mobley, Estimation of the remote-sensing reflectance from above-surface measurements, *Appl. Opt.* 38 (36) (1999) 7442–7455, <https://doi.org/10.1364/AO.38.007442>.
- [12] W. Ambarwulan, W. Verhoef, C.M. Mannaerts, M.S. Salama, Estimating total suspended matter concentration in tropical coastal waters of the Berau estuary, Indonesia, *Int. J. Rem. Sens.* 33 (16) (2012) 4919–4936, <https://doi.org/10.1080/01431161.2011.583289>.
- [13] P.N. Mahama, Assessment of the Utility of Smartphones for Water Quality Monitoring, University of Twente, 2016.
- [14] S. Novoa, H.J. van der Woerd, M. Wernand, Wacodi : a generic algorithm to derive the intrinsic color of natural waters from digital images, *Limnol Oceanogr. Methods* 13 (2) (2015) 697–711, <https://doi.org/10.1002/lom3.10059>.
- [15] M.R. Wernand, A. Hommersom, H.J. van der Woerd, MERIS-based ocean colour classification with the discrete Forel – ule scale, *Ocean Sci.* 9 (2013) 477–487, <https://doi.org/10.5194/os-9-477-2013>.
- [16] S. Novoa, M.R. Wernand, H.J. Van der Woerd, The Forel-Ule scale revisited spectrally: preparation protocol, transmission measurements and chromaticity, *J. Eur. Opt. Soc.* 8 (2013), <https://doi.org/10.2971/jeos.2013.13057>.
- [17] H.J. van der Woerd, M.R. Wernand, True colour classification of natural waters with medium-spectral resolution satellites: SeaWiFS, MODIS, MERIS and OLCI, *Sensors* 15 (2015) 25663–25680, <https://doi.org/10.3390/s151025663>.
- [18] S. Gert, Hermann Günther Grassmann (1809-1877): Visionary Mathematician, Scientist and Neohumanist Scholar, vol. 187, Springer Science & Business Media, Dordrecht, The Netherlands, 1996, <https://doi.org/10.1007/978-94-015-8753-2>.
- [19] R. Mabit, C.A.S. Araújo, R.K. Singh, S. Bélanger, Empirical remote sensing algorithms to retrieve SPM and CDOM in québec coastal waters, *Front. Remote Sens.* 3 (834908) (2022) 1–20, <https://doi.org/10.3389/frsen.2022.834908>.
- [20] E. Kari, et al., Retrieval of suspended particulate matter from turbidity – model development, validation, and application to MERIS data over the Baltic Sea data over the Baltic Sea, *Int. J. Rem. Sens.* 38 (7) (2017) 1983–2003, <https://doi.org/10.1080/01431161.2016.1230289>.
- [21] D.M.L. Horemans, Unraveling the Coupled Large-Scale Suspended Sediment and Phytoplankton Dynamics in a Turbid and Tide-Dominated Estuary, University of Antwerpen, 2022.
- [22] G. Neukermans, H. Loisel, X. Me, R. Astoreca, D. Mckee, In situ variability of mass-specific beam attenuation and backscattering of marine particles with respect to particle size, density, and composition, *Limnol. Oceanogr.* 57 (1) (2012) 124–144, <https://doi.org/10.4319/lo.2011.57.1.0124>.
- [23] A.I. Dogliotti, K.G. Ruddick, B. Nechad, D. Doxaran, E. Knaeps, A single algorithm to retrieve turbidity from remotely-sensed data in all coastal and estuarine waters, *Remote Sens. Environ.* 156 (2015) 157–168, <https://doi.org/10.1016/j.rse.2014.09.020>.
- [24] D. Stramski, E. Boss, D. Bogucki, K.J. Voss, The role of seawater constituents in light backscattering in the ocean, *Prog. Oceanogr.* 61 (2004) 27–56, <https://doi.org/10.1016/j.pocean.2004.07.001>.
- [25] A. Hatcher, P. Hill, J. Grant, Optical backscatter of marine flocs, *J. Sea Res.* 46 (2001) 1–12.
- [26] C.E. Binding, D.G. Bowers, E.G. Mitchelson-Jacob, Estimating suspended sediment concentrations from ocean colour measurements in moderately turbid waters; the impact of variable particle scattering properties, *Remote Sens. Environ.* 94 (2005) 373–383, <https://doi.org/10.1016/j.rse.2004.11.002>.
- [27] H.M. Dierssen, R.M. Kudela, J.P. Ryan, R.C. Zimmerman, Red and black tides: quantitative analysis of water-leaving radiance and perceived color for phytoplankton, colored dissolved organic matter, and suspended sediments, *Limnol. Oceanogr.* 51 (6) (2006) 2646–2659.
- [28] E. Boss, et al., Comparison of inherent optical properties as a surrogate for particulate matter concentration in coastal waters,” *Limnol. Oceanogr. Methods, Methods* 7 (2009) 803–810.